

Physical scaling in microstructures and avalanches of dislocation by Dislocation Dynamics simulations

Missipsa AISSAOUI, C. Kahloun, O.U. Salman, S. Queyreau

December 2024

Abstract

At the mesoscale, the avalanche-like plastic bursts are associated with statistical signatures, whose parameters are not always well defined. In this work, we performed large scale and realistic Dislocation Dynamics simulations of the deformation of fcc Cu in bulk systems under fixed strain rate. Our results show that the power law exponent is not impacted by the dislocation density nor the loading direction. However, dislocation density controls the scaling of the power law truncation in avalanche statistics and triggering stress at the origin of plastic events. The correlation between the activities of slip systems is highlighted. Our quantitative data can provide explanations for some experimental observations and help link the mesoscopic plasticity picture to larger-scale models.

Introduction

Plastic flow at the macroscale is known as a continuous process. However, as in many other physical phenomena, small-scale plastic deformation appears heterogeneous and intermittent, in the form of the avalanche-like phenomenon of plastic bursts. Plastic events $\delta\gamma$ follow the so-called power law distribution $P(\delta\gamma) \propto \delta\gamma^\alpha$. These avalanche statistics can be obtained through analysis of the discrete part of acoustic emission signals [1, 2, 3], or from the strain increments seen on the deformation curves obtained from simulations [4, 5, 6] or deformed pillars [7, 8, 9].

While power law (PWL) exponents found for 3D dislocation-based plasticity of fcc materials can well match those obtained for other non-equilibrium phenomena, the range of values is rather large, from -1 to -2.2 [7, 2, 10, 8, 6, 5, 11]. It is therefore unsure whether dislocation avalanches correspond to a single universality class [8]. Even when focusing on a single material, PWL exponent is shown to depend strongly upon the type of loading [6, 12] and imposed strain rate [8, 13]. Loading orientation may strongly impact the type of dislocation interactions and resulting dislocation microstructures, however the impact of orientation has been rarely studied. In [11], a PWL exponent $\alpha \approx -1.7$ was found to be independent of loading orientation in simulations of Discrete Dislocation Dynamics (DDD), while the exponent was found in experiments to vary from $\alpha \approx -1$ to -2 depending on the orientation of Au single crystals [8]. Assessing the organization of the dislocation microstructure through the triggering stresses at the origin of the avalanches could help in understanding the variety of critical exponents seen, however this analysis is typically hard to achieve [4, 14].

The pure PWL is known to be scale free, and a truncated PWL of the form $P(\delta\gamma) \propto \delta\gamma^\alpha \exp(-\delta\gamma/\delta\gamma_{max})$ is often employed to model the decreasing contribution of the largest plastic events [6, 13]. The determination of the PWL cutoffs is crucial in defining the average behavior and thus rigorously linking the mesoscopic picture of dislocation mechanisms to the continuous behaviour of materials at the macroscale. The PWL truncation is impacted by many parameters [6] like the amount of deformation [8, 10], single-crystal orientation [11, 5, 8] and imposed strain rate [6, 12, 13]. PWL truncation can make exponent identification more difficult, and its description is not yet fully quantitative.

Understandably, many existing experimental and simulation works focus on deformed micropillars in which the intermittency of plastic deformation is exacerbated. However, conventional dislocation mechanisms compete with the size effects induced in these finite-dimension systems [15]. On a macroscopic scale, PWL regimes and corresponding exponents are well defined over amplitudes or energies of up to five decades from the analysis of acoustic emission bursts [1, 2, 10], although the link with dislocation activity is not

direct. DDD simulations appear to be the simulation tool of choice, but few studies have focused on bulk systems in 3D [6, 5, 11, 14].

In this work, we show the changes in the dislocation avalanche statistics simulated by 3D Dislocation Dynamics simulations in the pure Cu bulk system. We focus on two microstructural parameters, namely: the dislocation density and dislocation microstructure through the crystal orientation, that may change material structure (disorder) and relative contributions of short- long-range contributions. Thanks to a careful simulation design, a large amount of data is obtained, enabling PWL regimes of up to five orders of magnitude to be unambiguously defined, bounded by well-defined cutoffs, clarifying some of the inconsistencies in the literature. Avalanche data are analyzed in greater detail to provide a unique picture of plastic deformation, such as the contribution of different slip systems, the distribution of critical configurations at the onset of avalanches and the correlation between systems. Characterization of the statistics enables quantitative modeling of avalanche statistics at the mesoscale, paving the way for new comparisons with experiments.

1 Methodology

We conducted a comprehensive study using large scale DDD simulations with the *microMegas* code, which has been described in details in [16, 17] and making use of the Cai et al.’s non-singular elastic theory [18, 19, 20]. This section only covers the specific conditions for the simulations carried out here.

In this study, we performed a series of model simulations of the tensile deformation of Cu single-crystals oriented along different directions leading to different slip activity and typical microstructures. Simulations encompass from [135] single-slip activation leading to dislocation entanglements, [112] double slip condition leading to planar microstructures, a latent hardening experiment [21, 22] for which the forest density is immobile and [001] stable multislip conditions building cells. This latter orientation is the focus of our study, as multislip condition is the dominant slip condition existing in polycrystals deformed at large strain. The elastic behavior of Cu is assumed to be linear and isotropic with a shear modulus $\mu = 42$ GPa and Poisson’s ratio $\nu = 0.34$.

In the absence of in-depth knowledge of the Frank’s initial network, the initial microstructure consists of a random distributions of dislocation prismatic loops with a length of $4 \mu m$ for segments in the primary systems and $1 \mu m$ for segments in the cross-slip system. This simulation cell has a linear dimension of approximately $L_B \approx 10\Lambda$, with $\Lambda \approx 1/\sqrt{\rho}$ following the *similitude principle* found in most of dislocation interactions and microstructures. Several initial realizations of the microstructures are considered, our analysis is limited to the simulations deemed the most realistic (e.g. with well-balanced slip activity leading to a stable loading direction). Periodic boundary conditions (PBC) are applied. Cross-slip for screw dislocations is controlled by a KMC algorithm following the model in [23, 24]. These arbitrary initial microstructures quickly evolve into realistic dislocation arrangements and this design has been successfully employed to quantify dislocation storage [5] or plastic hysteresis [25]

The dislocation density is varied over three orders of magnitude, starting from $\rho_0 = 0.5 \cdot 10^{10}$ to $2 \cdot 10^{12} \text{ m}^{-2}$ and deformation during a simulation typically leads to a significant increase of density of up to an order of magnitude. Dislocation density is changed in two ways: i) by starting with different microstructures while preserving the box dimensions, ii) by preserving the initial structure but resizing the entire geometry (and keeping $L_B = 10\Lambda$). Here, deformation is driven using a constant plastic strain rate $\dot{\epsilon}_a$, similar to strain driven experiments, with an infinite rigid machine stiffness. We carefully chose $\dot{\epsilon}_a = 50 \text{ s}^{-1}$ so as to preserve numerical efficiency while avoiding strain rate effects. In other words, deformation is solely controlled by forest interactions [26]. Our simulations reveal that the imposed strain rate has a dramatic impact on the avalanche statistics also seen in pillars [8, 13]. The influence of the loading rate on the plastic deformation at the mesoscale and dislocation avalanches’ signature is rather complex and nuanced, and this will be the subject of a forthcoming paper.

Great care has been paid to extract the most of and precise data from the simulations. For this, microstructure properties were saved at high frequency and high floating point precision. The presence of PBC may impact the largest plastic events. To correctly capture the natural maximal extension of avalanches and PWL truncation of avalanche statistics, we optimized the ratios of simulation box dimensions so as to obtain a very large extended slip plane -corresponding to the various tiles of slip plane swept by a dislocation loops while expanding (see. supplementary material). For a single slip system, The largest swept area free of any

PBC artifacts, can be as large as $\pi(65\mu m)^2$ for our multislip simulations and $\pi(95\mu m)^2$ for the single slip simulations. We will see that our simulation design allows large data sets, with about 20,000 plastic events per simulation, and well-defined statistical signatures.

Even with sufficient data, analyzing avalanche statistics can be a difficult task. Here, we reemploy and built upon the careful methodology derived by Clauset and coworkers [27]. To provide a quantitative description of the avalanche statistics from the simulations, most of our data is fitted using the robust maximum likelihood methodology by a truncated power law with an exponential decay (see supplementary material). The fits are based on data truncated beyond the lower $\Delta\gamma_{min}$ limit for the PWL regime. Curves (dashed lines) and fit parameters are generally shown in the figures.

2 Results

2.1 Impact of the dislocation density on avalanche statistics

Figure 1.a) shows some of the deformation curves obtained for the [001] orientation and different dislocation densities. The plastic behaviour is typical of pure Cu single crystals at room temperature [28, 24], with low flow stresses, a constant hardening rate of about $\mu/150$, and *normal* dislocation storage with $\sqrt{\rho} \propto \gamma$ the shear strain (cf. Fig. 1.b)) with very little dynamic recovery. In what follows, avalanche-like plastic bursts are characterized by a stress drop $\Delta\tau$ and strain increment $\Delta\gamma$ (see inset of Fig. 1.a)). Fig. 1.c) shows the amplitude of discrete events $\Delta\gamma_i$, whose number increase during microyielding and reaches up to 20,000 events at the end of a single simulation.

Next, we discuss the typical dislocation avalanche statistics focusing on plastic bursts $\Delta\gamma$ for reasons that will be explained later (stress resolved $\Delta\sigma$ analysis can be found in the Supp. Mat.). Figure 2.a) and .c) show the probability density function (pdf) of $\Delta\gamma$ as function of the initial dislocation density. The statistics exhibits an unambiguous power law regime $p(\Delta\gamma) \propto \Delta\gamma^{-\alpha}$ over a domain of up to four decades in event size, which is rarely seen in simulations. The exponent α in the PWL regime is about negative 1.6-1.7, similarly to what has been observed in previous 3D DDD in bulk systems [5, 11], and in the range of what is observed in experiments [8, 13, 10]. The exponent is clearly unchanged by the dislocation density, and this can be seen as in agreement with the data obtained on pillars deformed at different strain levels [8] or [10, 3].

Figure 1.c) shows that the stress drop $\Delta\tau$ and strain increment $\Delta\gamma$ are correlated, e.g. a large $\Delta\tau$ typically corresponds to a large $\Delta\gamma$. However, for small events, dispersions are very large. The correlation roughly follows $\Delta\tau \propto \Delta\gamma^\beta$ with $\beta = 1.43$ here. Interestingly, the exponent of correlation β is unaffected by dislocation density nor loading conditions (see below). This constant correlation justifies our focus on strain resolved $\Delta\gamma$ data.

Now, let us focus on the bounds delimiting the PWL regime. The cutoffs are best seen on the complementary cumulative distribution function (ccdf) shown in Fig. 2.b) and d). To give a sense of the size of plastic events simulated, we define an avalanche extension metric L defined from Orowan's law as $L^2 = \delta\gamma Vol/b$, with Vol the simulated volume. The size of avalanches $\delta\gamma$ defined in this metric is also provided in the figure 2. Following the idea of Kubin and collaborators, the average of $\langle L \rangle$ is expected to be connected to the so-called Mean Free Path of dislocations [5], although the explicit relationship has yet to be found.

The statistics obtained from our carefully designed simulations present well defined PWL bounds, which is not always the case in the literature. Here, the smallest strain bursts $\min(\delta\gamma)$ are independent from the dislocation density and of about 3.10^{-8} . This is equivalent to $L^2 \approx (0.05\mu m)^2$, which corresponds certainly to very small displacements of an individual dislocation (see next section). The largest events, are also well defined in our analysis, and the cutoff $\delta\gamma_{max}$ is strongly impacted by the dislocation density as $\max(\delta\gamma)$ goes from 3.10^{-4} to 2.10^{-5} when the initial dislocation density increases from $\rho_0 = 5.10^{10}m^{-2}$ to $2.10^{12}m^{-2}$. The maximal size of the simulated avalanches reaches $L^2 \approx (30\mu m)^2$ (in the fixed-dimension box), which is several times the box dimensions yet smaller than the extended plane dimensions. We will thus consider that $\max(\delta\gamma)$ represents the *maximal natural extension* of dislocation avalanches.

Here, our results cover both of our simulation design strategies : i) fixed-box dimensions with increased dislocation densities and ii) resized simulation boxes. The impact of dislocation density on the PWL bounds is found to be coherent and similar in both sets of simulations (when accounting for the difference in total strain reached), therefore independent of the modeling strategy. In 2D simulations, homothetic box geometries are sometimes employed [4], to vary dislocation density, while preserving the initial relative positions of

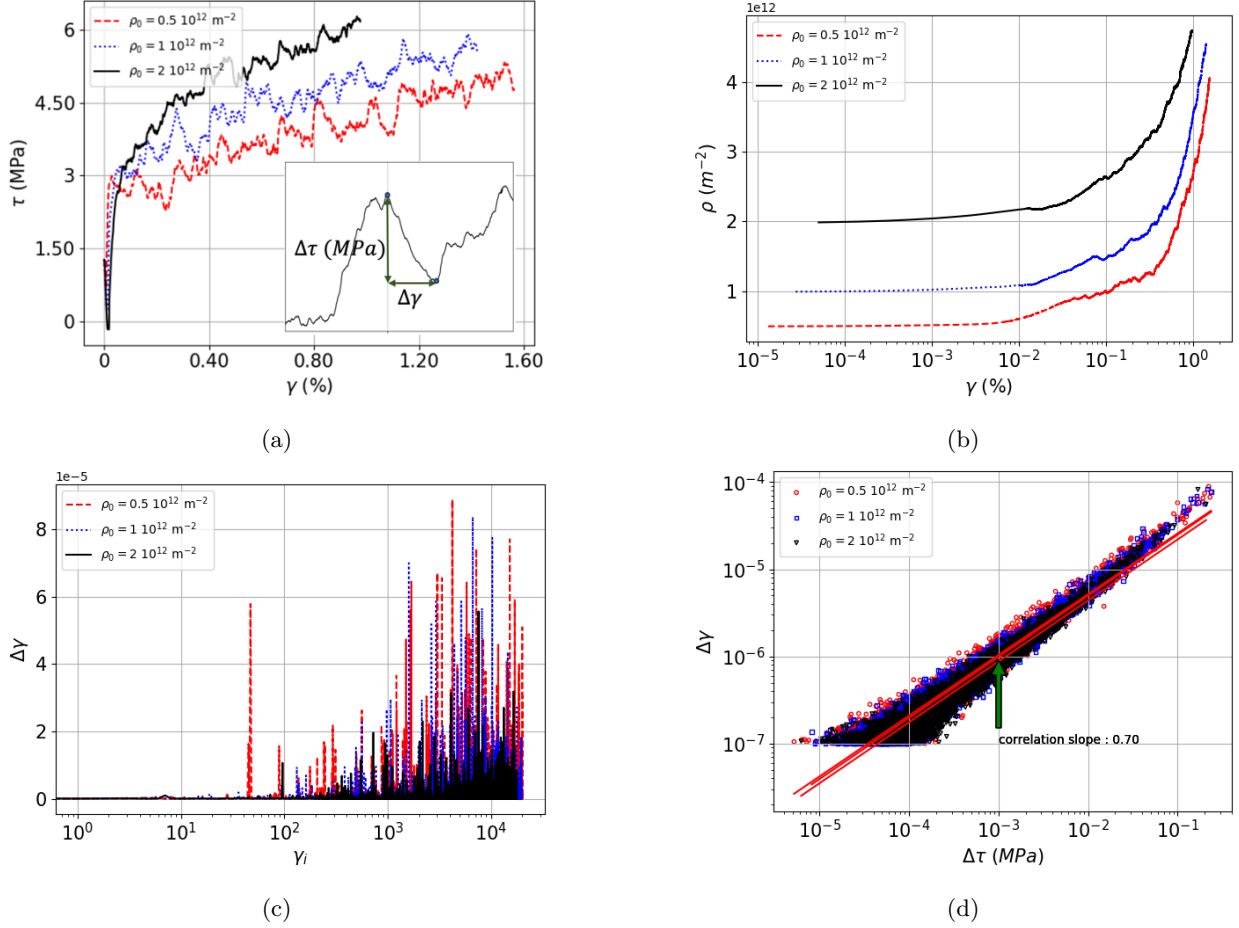


Figure 1: Typical mesoscopic plastic behavior simulated by DDD for Cu [001] single crystals under constant strain rate. (a) Deformation curves with the shear stress τ as function of the total shear strain γ for different initial density ρ_0 . Inset: zoom in on one of the serrations seen on the deformation curve. We define the strain-bursts $\delta\gamma$ and the stress-drop $\delta\tau$ for every plastic events. (b) Corresponding evolutions of the dislocation density $\rho(t)$ as function of the total shear strain γ . (c) Amplitude of individual strain-bursts $\delta\gamma$. (d) Correlation between the strain-bursts $\delta\gamma$ and the stress-drop $\delta\tau$, for $\delta\gamma > 1.10^{-7}$, well into the PWL regime.

segments. Deformation is expected to proceed in similar successions of configurations. However, in massive 3D simulations such as those carried out here, junction stability and cross-slip activity may be rather different when physical dimensions are rescaled. In consequence, the succession of plastic events is different even when starting from the same -albeit rescaled- dislocation microstructure. Simulations with homothetic box geometry are however more numerically efficient, and large deformation and densities can be achieved.

2.2 Influence of the loading direction on avalanche statistics

In this second set of simulations, the simulated microstructures are modified by deforming single crystals along different orientations. The initial dislocation density is taken as $\rho_0 = 10^{12} \text{ m}^{-2}$. Several realizations of the initial microstructure are considered, we have kept the one associated with a plastic deformation balanced between the different active slip systems, leading to the hardening rate expected from experiments. For the sake of brevity, the deformation curves and the evolution of the dislocation density curves are collected in the supplementary materials.

Avalanche signatures displayed in Figure 3 for these new conditions share many of the features discussed

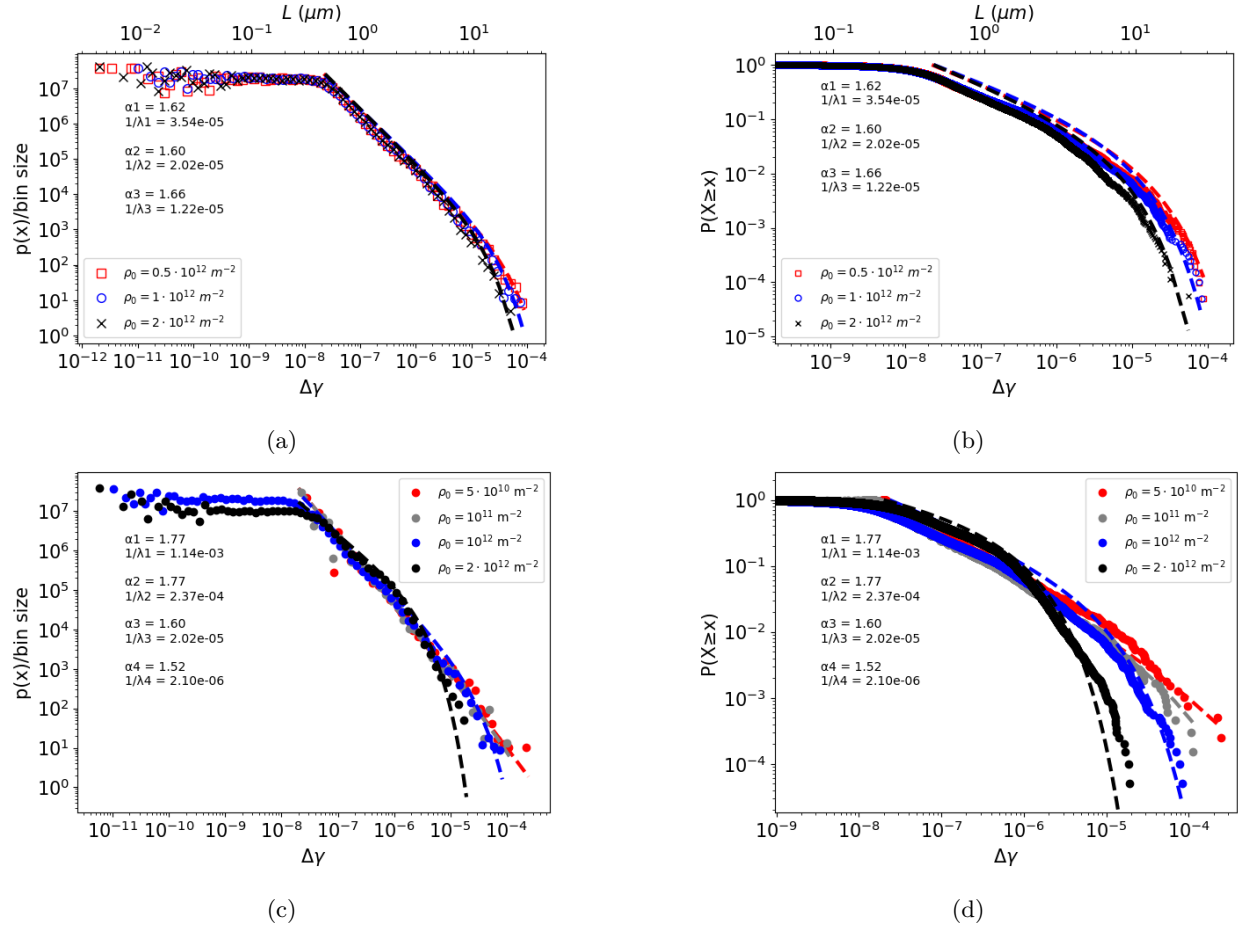


Figure 2: Impact of the dislocation density upon the strain resolved avalanche statistics during [001] deformation of Cu single crystals. (a) and (c) Probability density function (PDF) of strain-bursts $\delta\gamma$ ($= x$). The avalanche extension L is also given in units of μm (see main text). Complementary stress resolved data are provide in Supp. Mat. (b) and (d) Complementary cumulative probability function of strain-bursts $\delta\gamma$. For a) and b), the box dimensions are fixed and dislocation density is changed. For c) and d), box dimensions are resized changing the dislocation density while preserving the numerical efficiency of DDD simulations at large densities.

previously. Irrespective of the orientation, an extended PWL regime is found and associated to a similar critical exponent $\alpha \approx -1.5$ to -1.7 . We focus on strain-resolved data because the approximate correlation between stress drop-strain burst is still operative $\Delta\tau \propto \Delta\gamma^\beta$ and unchanged by loading direction. Stress resolved data can be found in the supplementary materials. PWL domain is delimited by well defined bounds. The lower cutoff $\Delta\gamma_{min}$ seems to be slightly dependent upon the loading direction but more significant is the strong dependence of the upper truncation of the PWL regime $\Delta\gamma_{max}$, which is clearly anisotropic. $\Delta\gamma_{max}$ clearly decreases as the number of active slip system increases. In agreement with previous results, largest avalanches probability decreases as obstacle density increases.

A similar qualitative trend has been observed in a few of other studies from the literature. For example, Devincre and collab. found similar exponents for [135], [112], [111] and [001] single crystals by means of 3D DDD simulations on bulk systems [11], the PWL regime and its bounds are however less well-defined. In an experimental study on Au micropillars [8], Sparks and Maa β obtained decreasing PWL exponent from -1 to about -2 when considering loading directions of increasing symmetry ranging from [123], to [001]. The difference with our findings is not yet fully understood, but could be explained in part by the evolution of the cutoffs with dislocation density. Next, we will present an analysis of what constitutes an avalanche in

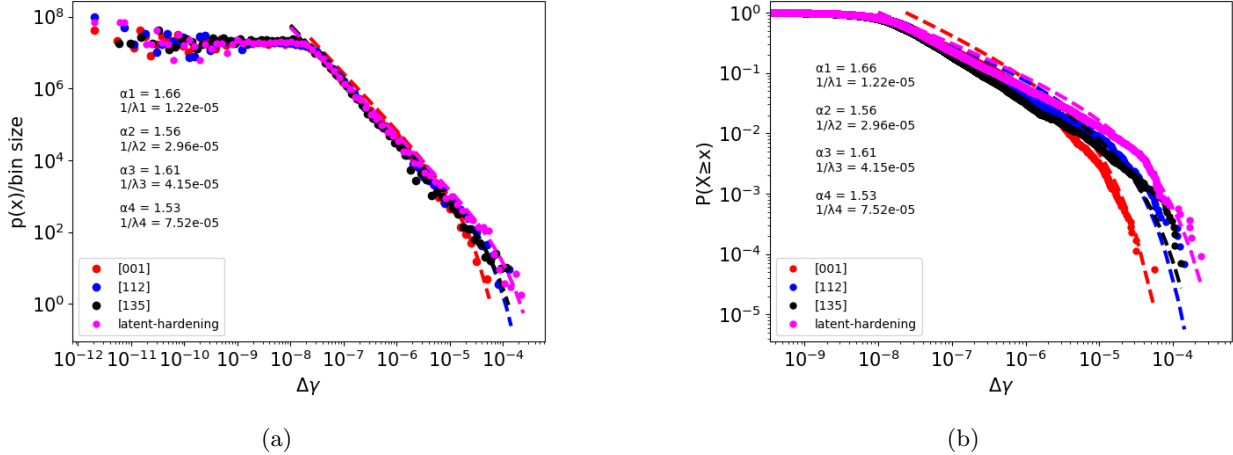


Figure 3: Impact of the loading conditions on the avalanche statistics. (a) Probability density function (PDF) of strain-bursts $\delta\gamma$. (b) Complementary Cumulative Distribution Function (CCDF) of strain-bursts $\delta\gamma$

our DDD simulations so as to be able to define the evolution of the PWL cutoff $\Delta\gamma_{max}$.

A decrease of avalanche size as the density of obstacles blocking the dislocations increases is rather natural. However, this has two main consequences. i) In both simulations and experiments, dislocation density increases monotonically, which means that the resulting avalanche statistics are in fact associated to a constantly changing PWL cutoff. ii) Since avalanches occur on localized slip planes, it is questionable which part of the dislocation microstructure will actually contribute to stopping avalanches.

2.3 Individual slip system contribution to avalanches

Here, we propose a complementary look at the statistical signature of avalanches on a per-system basis. Due to the shared statistical signatures of the phenomenon belonging to the same universality class, details of the physical mechanisms associated with avalanches are generally considered unimportant in the literature. However, these details of underlying interactions may well become essential for characterizing PWL truncations and provide valuable information for future larger-scale modeling.

From the observation of simulation sequences, we know that dislocation avalanches may be initiated by various *critical events* such as: i) a single segment acting akin to a source, ii) destruction of binary or higher order junctions, iii) or snow-balling effect. Tracking these events directly as the simulated microstructure evolves is virtually impossible at the moment. Here we propose instead a statistical analysis of the relative contributions of individual slip systems 's' though the ratio $c_{sa} = \frac{\Delta\gamma_s \in a}{\sum_j |\gamma_j| \in a}$ to an individualized avalanche 'a'. Avalanches are further categorized into three different bins (with similar event numbers) depending on their overall size: small strain bursts with $\delta\gamma < 2.10^{-7}$, intermediate avalanches in the PWL regime with $2.10^{-7} < \delta\gamma < 3.10^{-6}$, and the largest avalanches above $\delta\gamma > 3.10^{-6}$.

Histograms of c_{sa} are provided for all primary and cross-slip systems in Fig. 4 for a [001] simulation, representative of other simulations. Typically, small plastic events correspond to quantized contributions of the different active slip systems. Very often, not all systems contribute to small events ($c_{sa} = 0$), other times, only one system is contributing alone to the avalanche ($c_{sa} = 1$). Between these extremes, n slip systems share similar contributions to $\delta\gamma_a$ with peaks around $c_{sa} = 25\%$, 33% or 50% ($\approx 1/n$). This contrasts greatly with the continuous histogram obtained for the largest avalanches, where a single system cannot contribute alone ($c_{sa} = 1$) and fewer cases of inactive slip systems can be found. Most of these large plastic events correspond to concomitant activity on all slip systems, with a broad peak around $c_{sa} \approx 25\%$. This picture of large events where all slip systems are contributing from the beginning or when destabilized by activity in an adjoining region, matches well the general picture of avalanches. Finally, the histogram for intermediate events, in the middle of the PWL regime corresponds nicely to a mixture of the two previous histograms. Besides, cross-slip systems tend to contribute in average less to avalanches. Correlations among slip system

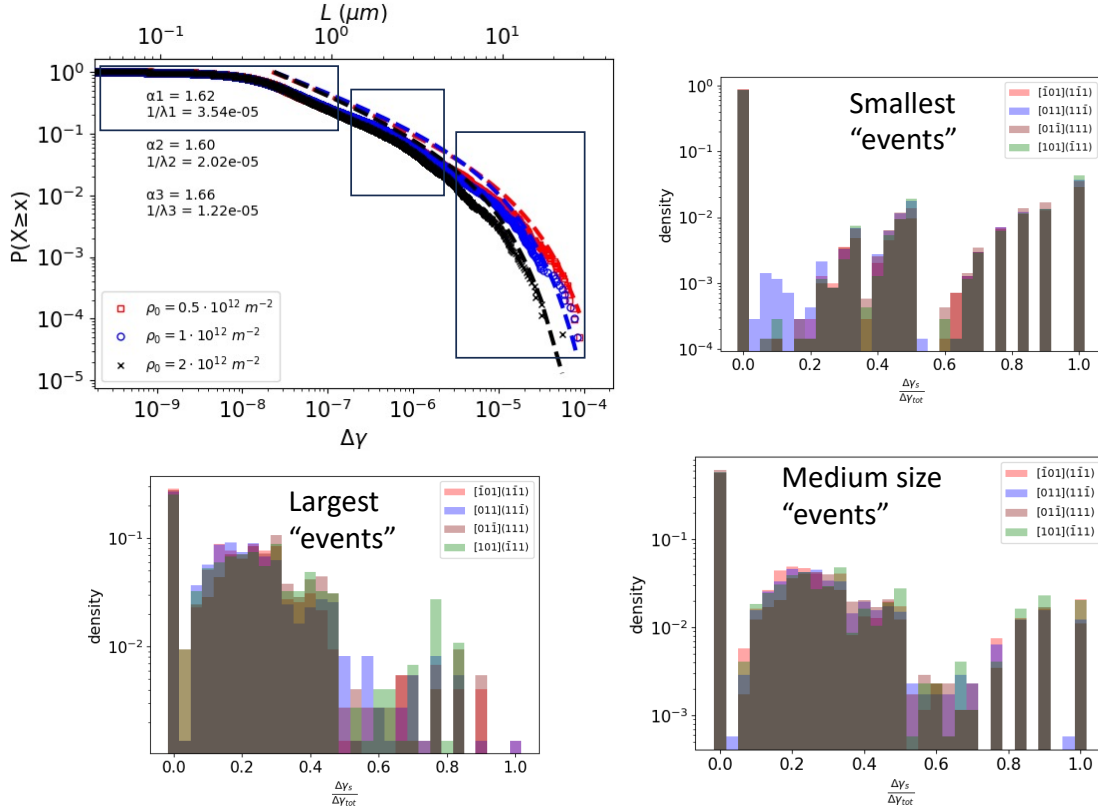


Figure 4: Histograms of avalanche contributions $c_{s\alpha}$ for the four stable primary systems in a [001] simulation at $\rho_0 = 10^{12} \text{ m}^{-2}$. Histograms are further separated into three bins depending upon the size of the avalanches shown on the top left: (a) small plastic bursts, (b) intermediate avalanches well in the PWL regime and (c) largest avalanches.

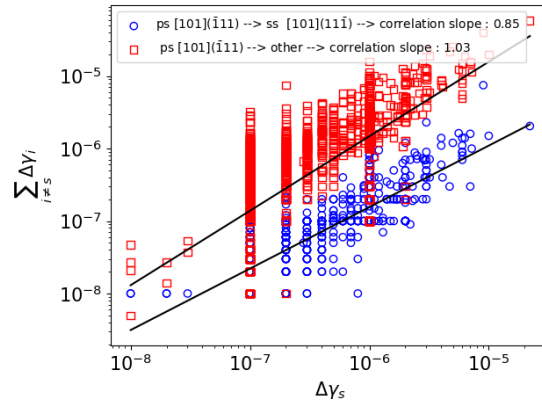


Figure 5: Correlations among slip system contributions to avalanches. Correlation (blue) between the primary system $1/2 [-101](1-1 1)$ and its cross-slip system $1/2[-101](111)$; correlation (red) between the primary system $1/2 [-101](1-1 1)$ and all other systems except its cross-slip system $1/2[-101](111)$.

activities (even when unactive) were also recently nicely illustrated in [29], here we show that this correlation is rooted in the avalanche kinetics itself.

Figure 5 further illustrates the correlations existing among slip systems, where $\Delta\gamma_s$ is plotted as function

$\sum_{j \neq s} \Delta\gamma_j$. An approximate correlation is found $\Delta\gamma_i \propto \Delta\gamma_{j \neq i}^{1.06}$ with admittedly a large spreading of the data. Surprising also is the slightly different correlation found between the primary and cross-slip systems as $\Delta\gamma_i \propto \Delta\gamma_{CS_i}^{0.9}$. We expect that a plastic burst on a primary segment will carry with it the superjogs or cross-slip segments that were already present on the initial dislocation [30]. This reduced correlation thus suggests that cross-slip activity is in competition with the primary system.

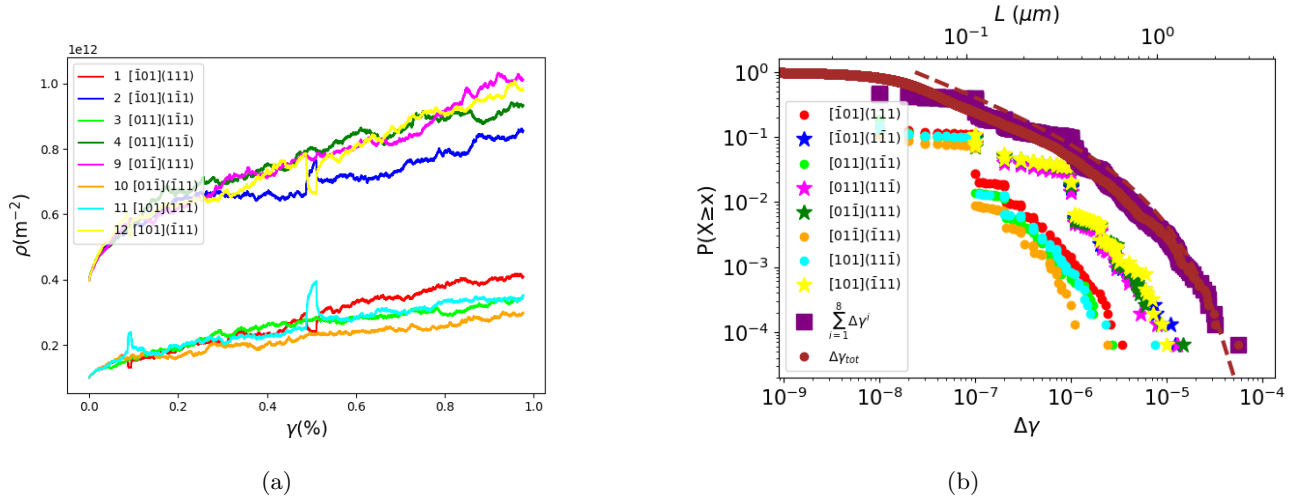


Figure 6: Statistical analysis of dislocation avalanches on a per-system basis. a) Evolution of the dislocation density on the four different primary and corresponding cross-slip systems during deformation along [001] direction. b) CCDF for $\Delta\gamma_i$ on each of the active slip systems are compared with the global CCDF. Fewer plastic events are found on the cross-slip systems (lower curves) since the initial microstructure is made of asymmetrical prismatic loops to ensure loading stability along the [001] direction. Floating point precision is lower for $\Delta\gamma_i$ than what was used for $\Delta\gamma$.

Finally, Figure 6 shows the CCDF for plastic bursts $\Delta\gamma_i$ on individual systems 'i'. The statistical signature is similar to the distribution obtained previously for the total plastic bursts $\Delta\gamma$. The extend of the PWL regime is shorter as events are smaller, PWL exponent is close to 1.5 for both primary and cross-slip systems. Naturally, we can show that $pdf(\Delta\gamma_{tot}) = pdf(\sum \Delta\gamma_i)$ (also true for the CCDF). However, $pdf(\Delta\gamma_{tot}) \neq \sum pdf(\Delta\gamma_i)$ as correlations exist among slip system strain bursts (see above). Ultimately, it becomes clear from the figure that $\max(\Delta\gamma_i)$ are different for every slip systems as dislocation densities are not exactly the same on all primary or all cross-slip systems as commonly seen at the mesoscale.

2.4 Scaling of cutoff $\Delta\gamma_{max}$ with dislocation density and orientation

Simulation results clearly show that the PWL truncations decreases with the increase of the density of obstacles seen by avalanches. The pure PWL is known to be scale free, therefore understanding the cutoffs of the PWL regime becomes important to be able to define average processes of the intermittent plastic activity seen at the mesoscale and provide a rigorous derivation of plastic behaviour at the continuous macroscale. Since dislocation density evolves continuously in simulations and experiments, the cutoff $\Delta\gamma_{max}$ is ill defined, which may explain in part the wide fluctuations seen in the literature.

Our results also provide a physical justification for the functional employed to model avalanche statistics. Avalanche extension is controlled by the collisions with forest obstacles, and collisions between dislocations show similarities with 1D Poisson processes [31]. Truncating the PWL with an exponential decay is thus very appropriated: $pdf(\delta\gamma) \propto \delta\gamma^\alpha \exp(-\lambda\delta\gamma)$ with $\lambda = 1/\delta\gamma_{max}$ parameters resulting from the modeling of the DDD data ($\delta\gamma_{max}$ is a fitting parameter and not exactly $\max(\delta\gamma)$ from DDD data). We will continue using this functional to model avalanche statistics.

To quantify the evolution of the $\delta\gamma_{max}$ during a single simulation, we need to assess it over a range of events, that is small enough so that the dislocation density increase can be neglected, while preserving

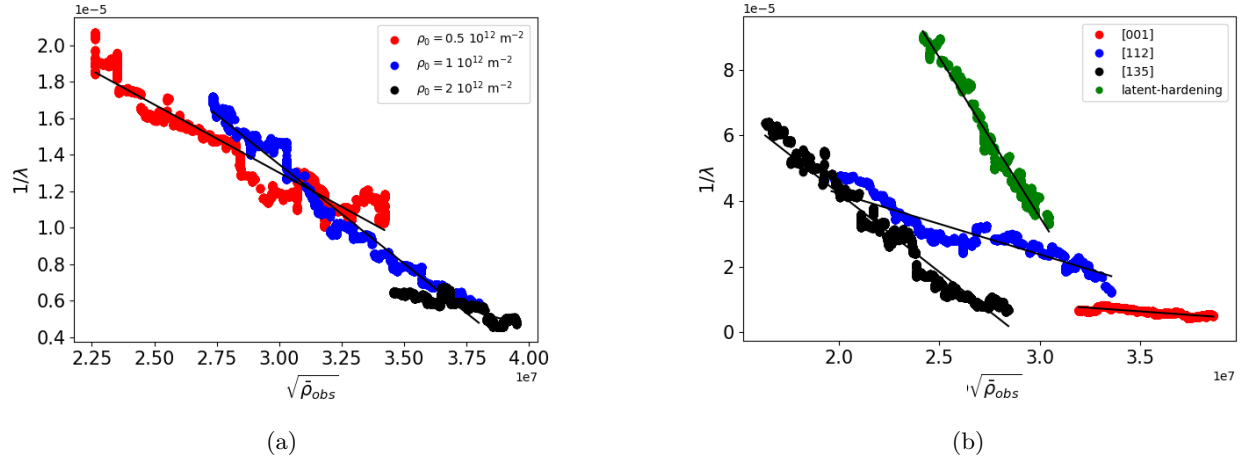


Figure 7: Evolution of the parameter $\delta\gamma_{max} = 1/\lambda$ modeling the PWL upper cutoff. It is calculated by means of a sliding window of 6,000 events, for which the dislocation density evolution is negligible. $\delta\gamma_{max}$ is shown as function of $b\sqrt{\bar{\rho}_{obs}}$. a) Results for various [001] simulations at different initial dislocation density. b) Anisotropy of the $\delta\gamma_{max}$ evolution, which depends upon the loading direction.

statistical significance. We will thus fit the avalanche data using a running window over a finite number of plastic events. This is made possible thanks to the large data available here. We varied the size of the running window from 700 to 10,000 events, the resulting quantitative $\delta\gamma_{max}$ evolution is impacted by less than 10%, which is deemed enough for the present study's goal.

Figure 7 shows the evolution of the $\delta\gamma_{max}$ parameter fitted using MLE from the DDD data. Since $\delta\gamma_{max}$ must correspond to a shear, we propose that it scales as $\propto b\sqrt{\bar{\rho}_{obs}}$. Here, we defined $\bar{\rho}_{obs}$ as a weighted average of the forest density seen by the systems 'i' participating to the avalanches 'a' under considerations: $\rho_{obs}^i = \sum_{j \neq i} \rho_{obs}^j$, and $\rho_{obs}^\alpha = \sum_i c_{ia} \rho_{obs}^i$. The results are not so different from the simpler average over the dislocation forest density $\rho_{obs}^i = \sum_{j \neq i} \rho_{obs}^j$. Starting with the [001] data under different initial dislocation density, $\delta\gamma_{max}$ clearly decreases $\delta\gamma_{max} \propto -C_{hkl} b\sqrt{\bar{\rho}_{obs}}$, with a nice overlap between simulation data. λ evolves monotonically, which means that the avalanche statistics (or at least the cutoff) is rapidly converging to that associated with deformed dislocation microstructures. Finally, when considering other loading conditions, the scaling of $\Delta\gamma_{max}(\rho)$ remains negative but appears anisotropic as C_{hkl} depends upon the orientation. This anisotropy is in agreement with [11, 8].

2.5 Distribution of avalanche triggering stresses τ_c :

In this last section, we show that dislocation density not only controls the scaling of avalanche statistics cutoffs but also the critical configurations at the origin of avalanches. The onset of avalanches corresponds to a unique situation when the applied loading equals the critical stress to activate a configuration within the dislocation microstructure. This is a critical stress, since the stress increase that precedes has mostly an elastic origin (along with perhaps a slight dislocation curvature increase), and past that stress, the activated dislocation segments are not under mechanical balance, the resulting effective stress leads to large instantaneous velocity [26].

Quantifying the distributions of *-triggering stresses-* is crucial to understand microstructure organization and the related disorder at the origin of avalanches. This is another ingredient required to rigorously bridge the discrete nature of plastic deformation at the mesoscale to the continuous picture at the macroscale. Quantifying these distributions is however rather hard to achieve in practice as large fluctuations may be obtained [4, 14].

Focusing on the [001] multislip conditions, we analyze the distributions of triggering stresses for different deformation states starting with an initial dislocation density $\rho_0 = 10^{12} \text{ m}^{-2}$. To help characterizing these distributions, we also performed a fit using a Generalized Extreme Value (GEV) probability distribution, which are displayed on the Figure 9. The raw distributions are prone to large statistical fluctuations similarly

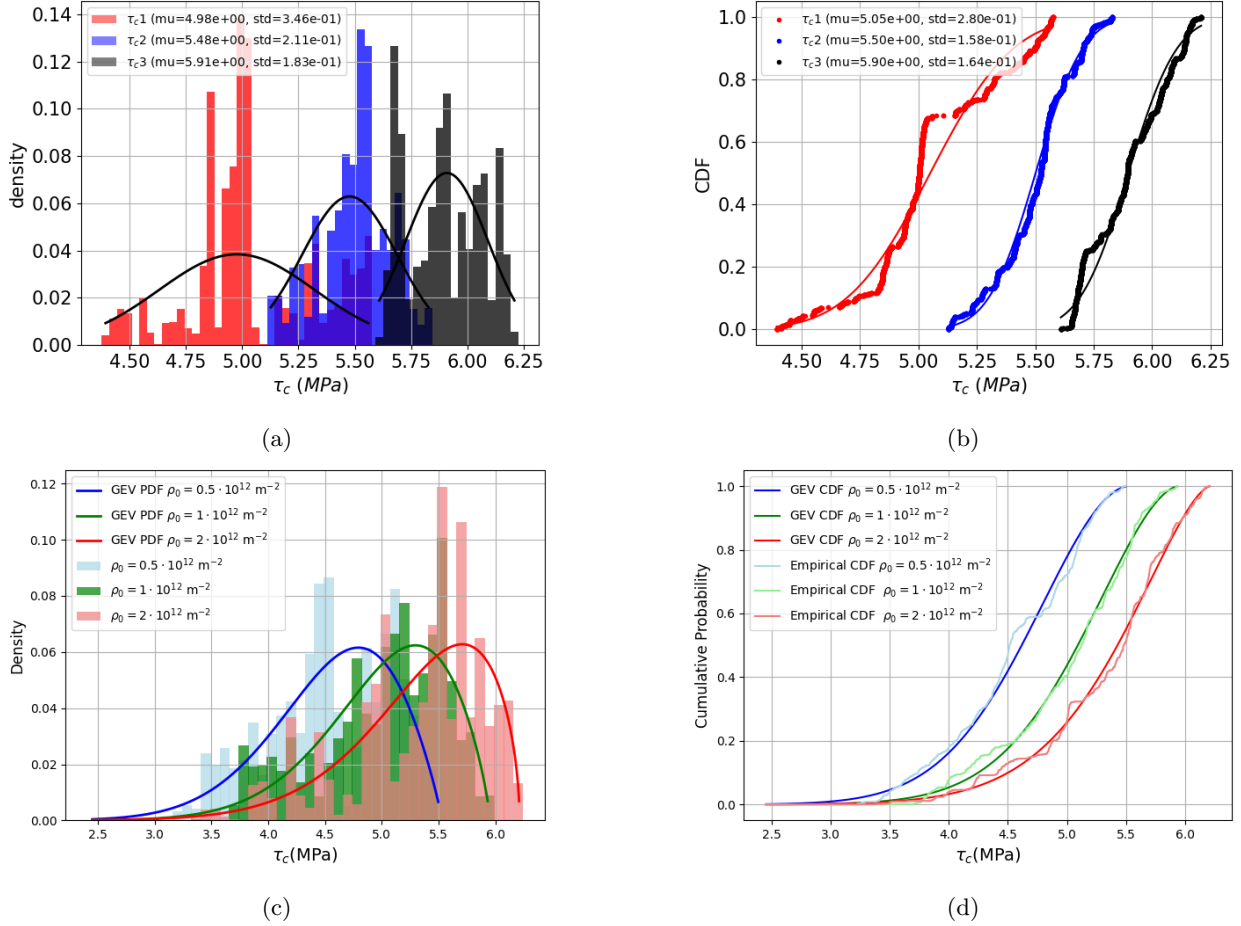


Figure 8: Raw histograms of triggering stresses τ_c measured in [001] deformation simulations. (a) and (b) correspond to histograms obtained during deformation with an initial dislocation density of $\rho_0 = 10^{12} \text{ m}^{-2}$. Three ranges of deformation are considered here corresponding to different deformation states: beginning of the deformation for $\gamma < 0.46$ (in red), intermediate range for $0.46 < \gamma < 0.73$ (in blue), and final range of the simulation for $\gamma > 0.73$ (in black). The resulting bins accounts for about the same number of events. (c), (d) regroup histograms for [001] deformation starting with different initial dislocation densities (cf. deformation curves in Fig. 1). (a) and (c) are to density histograms, while (b) and (d) correspond to cumulative histograms.

to past attempts of this kind [4]. However, the distributions are peaked for a τ_c values that increase with deformation, in agreement with the hardening observed. Distributions becomes less spread and more peaked as deformation progresses. This means that critical configurations associated to larger τ_c develop during deformation, and their relative contribution to the dislocation microstructure increases.

The analysis of the triggering stress distributions in Fig. 8.(c) and (d) for different initial dislocation densities provide a similar picture. The distributions are better defined as the data for each simulation is now analyzed as a whole (with about 20,000 configurations). Histograms become less spread, more peaked, and shifted to larger stresses as the dislocation density increases. The distributions are slightly asymmetrical as they would correspond to a GEV distribution with a long tail on the low stress side.

The striking similarities among the distributions suggest that a common distribution may exist. The average stress is known to follow the classical dimensionality scaling $\bar{\tau}_c \propto \mu b \sqrt{\rho_{obs}}$ when plastic flow is controlled by dislocation reactions [32, 33, 34, 35]. Figure 9 shows that all histograms converge toward the same underlying distribution when rescaling the triggering stress by $\sqrt{\rho_{obs}}$. The distribution can thus be

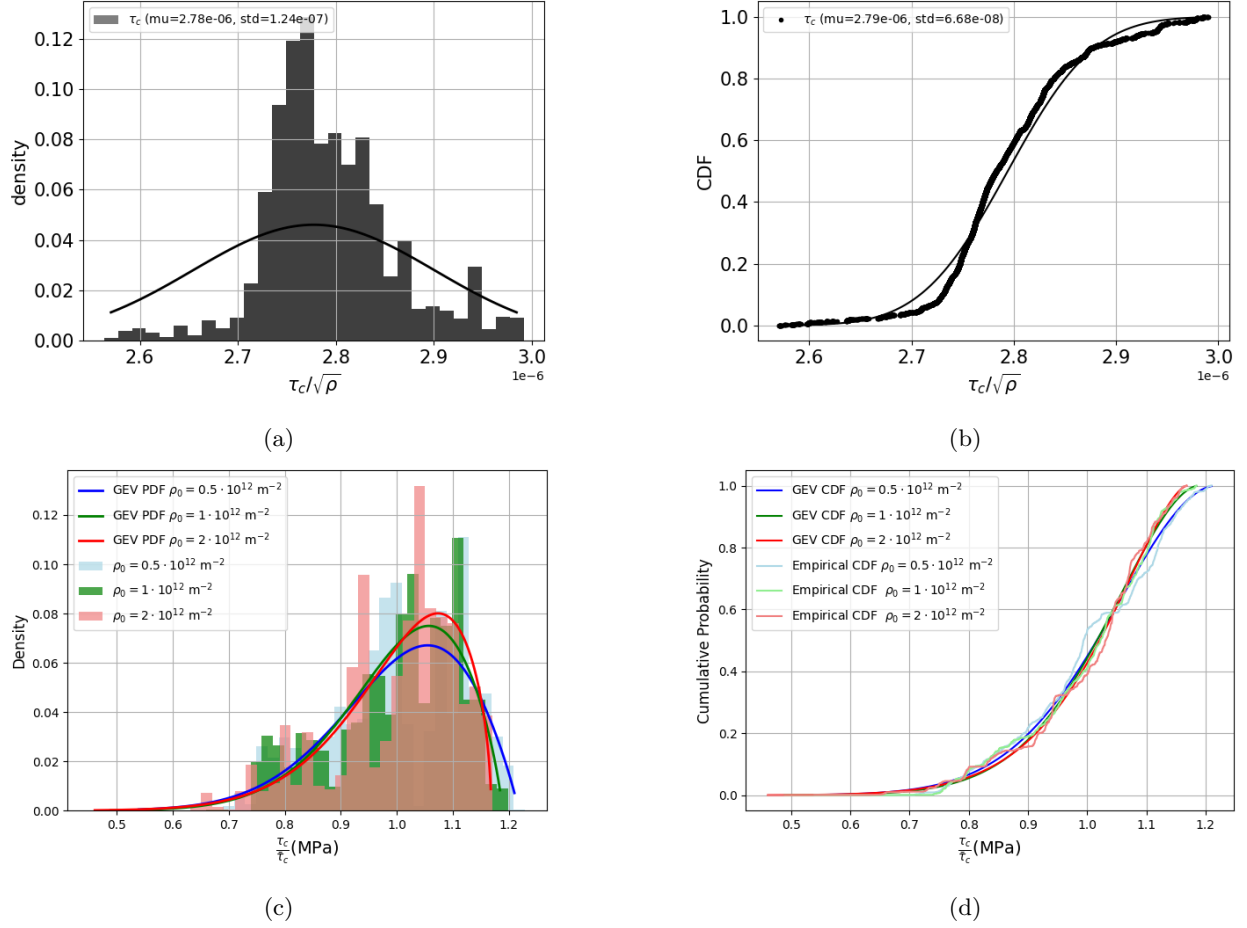


Figure 9: Histograms of triggering stresses τ_c rescaled by $\sqrt{\rho_{obs}}$. The subfigures mirror the presentation of previous figure with (a) and (b) correspond to histograms obtained during deformation with an initial dislocation density of $\rho_0 = 10^{12} \text{ m}^{-2}$. (c), (d) regroup histograms for [001] deformation starting with different initial dislocation densities.

written as :

$$f(\tau_c) = \frac{k}{\bar{\tau}_c} \left(\frac{\tau_c}{\bar{\tau}_c} \right)^{k-1} \exp\left(-\left(\frac{\tau_c}{\bar{\tau}_c}\right)^k\right)$$

This suggests that the organization of the dislocation microstructure (or at the minimum, the critical configurations) remains the same during deformation. The full study of these distributions, their properties and how they relate to the dislocation microstructure in its entirety is outside the scope of this paper, and will be the topic of an upcoming paper.

Concluding remarks

The present paper reports a comprehensive study to assess the impact of two microstructural parameters -the dislocation density and crystal orientation- on the avalanche statistics in bulk fcc Cu deformed under a fixed strain rate. Our strain resolved simulation results evidence a well defined PWL regime with an exponent α between -1.6 to -1.7, which is in the range of exponents seen for dislocation plasticity in 3D [1, 2, 8, 5]. The exponent is unaffected by dislocation density and loading conditions suggesting that these parameters have no impact over the associated class of universality. These parameters can thus be ruled out as an explanation for the variation in PWL exponent observed in the literature. For a given material, the PWL exponent is only controlled by the imposed strain rate [8, 36] our forthcoming paper. We can therefore conclude that the exponents obtained in the case of polycrystals made up of aggregates of grains of potentially different dislocation densities and orientations are well defined as long as the strain rate inside the grains where avalanches are active is the same. This condition is generally considered to be true at small strain, but may not apply in latter stages of deformation.

The relative importance of short- and long- range contributions to interactions was expected to impact avalanche statistics. For the former, a small effect was expected, as the self-stress scaling with dislocation density (through $l \propto 1/\sqrt{\rho}$) while not formally the same, is not so far from the scaling of long-range elastic contributions with density. However, a stronger impact was expected from the different loadings and deformation paths considered here. Single glide deformation is typically associated to strong multipolar distant interactions within the entanglements formed, with few reactions associated to collision with collinear superjogs [30]. This contrasts with [112] and [001] multislip conditions where plastic flow proceeds with a large number contact reactions and are associated to the formation of planar or cellular microstructures. Finally, the latent hardening simulation is very different from the previous conditions as the part of the microstructure corresponding to the inactive forest systems is imposed from the start, and should not evolve significantly.

Our data shows that the PWL truncation can be modeled as $\Delta\gamma_{max} = D_{hkl} - C_{hkl}b\sqrt{\rho_{obs}}$. This result is in qualitative agreement with the scaling suggested by Csikor and collaborators [6] from simulation and experimental data as:

$$\Delta\gamma_{max} \propto \frac{bE}{D(\theta + M)} \quad (1)$$

where E is the Young's modulus, θ a hardening strain rate, and M the combined stiffness of the both the specimen and the testing machine. The length D is microstructure dependent and can be used to capture size effects as the one we obtained here. Dislocation microstructures follow the *similitude principle* and typically scales as $D \propto 1/\sqrt{\rho}$, which is thus in agreement with our findings. Besides, in the expression above $\Delta\gamma_{max} \propto 1/D(\theta + M)$, and this is also consistent with the lower value that were obtained for C_{hkl} in multislip conditions and the corresponding large hardening.

The dependence of the cutoff with dislocation density has several consequences. First, most of the existing data from simulations or experiments has been obtained during deformation, and depending on the system, dislocation density may have largely increased. The measured avalanche statistics is thus a superposition of an evolving distribution. This could cause some roundness in the PWL regime or difficulty to define the cutoff of the distribution. Second, The avalanche statistics is therefore a function of both $\delta\gamma$ and ρ_i :

$$pdf(\delta\gamma, \rho) \propto \delta\gamma^\alpha \exp(-\delta\gamma/\delta\gamma_{max}(\rho)) \quad (2)$$

And this pdf should be formally integrated if ρ is not constant, therefore changing the normalization constants. Finally, in some experimental works [3], acoustic emission signals are separated into a continuous AE signal associated to a Gaussian distribution of amplitudes for which plasticity is mild, and discrete AE signal associated to a PWL regime for which plasticity is wild. As deformation proceeds, the wild part of the signal diminishes. Our quantitative results confirm the interpretation from the authors [3], as the discrete part of plastic flow that can be detected by AE, (that is above the background threshold and below the PWL cutoff) has to decrease.

Supplementary Material

Avalanche analysis and modeling

Dislocation avalanche amplitudes [5, 37] typically follow a power law distribution of the form $p(x) = Cx^{-\alpha}$. Power law analysis may be delicate when seeking for quantitative results, here, we mostly reprise the approach from [27]. We will employ a truncated PWL distribution with an exponential decay: $p(x) = Cx^{-\alpha}e^{-\lambda x}$. two parameters need to be defined: α and λ [27].

The complementary cumulative distribution function (CCDF), provides a complementary view of a variable distributed according to a power law, denoted as $P(x)$, which for the continuous case is defined as $P(x) = \Pr(X \geq x)$:

$$P(x) = \int_x^{\infty} p(x') dx' = \left(\frac{x_{\min}}{x}\right)^{\alpha-1}. \quad (4)$$

Generally, the visual shape of the CDF is more robust than that of the probability density function (PDF) against fluctuations due to finite sample sizes, especially in the tail of the distribution.

Considering the continuous power-law distribution:

$$p(x) = (\alpha - 1)x_{\min}^{\alpha-1}x^{-\alpha}, \quad (5)$$

where α is the scaling parameter and x_{\min} is the minimum value from which the power-law behavior is observed. Given a dataset containing n observations $x_i \geq x_{\min}$, we would like to determine the value of α for the power-law model that is most likely to have generated our data. The probability that the data are drawn from the model is proportional to

$$p(x | \alpha) = \left(\frac{\alpha - 1}{x_{\min}}\right)^n \prod_{i=1}^n \left(\frac{x_i}{x_{\min}}\right)^{-\alpha}. \quad (6)$$

This probability is the likelihood of the data given the model [27]. The data are most likely to have been generated by the model with the scaling parameter α that maximizes this function. In practice, we often work with the logarithm L of the likelihood, which reaches its maximum at the same point:

$$\begin{aligned} L = \ln p(x | \alpha) &= n \ln(\alpha - 1) - n \ln x_{\min} - \alpha \sum_{i=1}^n \ln \left(\frac{x_i}{x_{\min}}\right) \\ &= n \ln(\alpha - 1) - n \ln x_{\min} - \alpha \sum_{i=1}^n \ln \left(\frac{x_i}{x_{\min}}\right). \end{aligned} \quad (7)$$

By setting $\frac{\partial L}{\partial \alpha} = 0$ and solving for α , we obtain the maximum likelihood estimate (MLE) for the scaling parameter:

$$\hat{\alpha} = 1 + n \left[\sum_{i=1}^n \ln \left(\frac{x_i}{x_{\min}}\right) \right]^{-1}. \quad (9)$$

Tessellation of the extended slip planes

The use of periodic boundary conditions may lead to known artifacts, the main one being the self interaction of an expanding loop with itself [38]. Preventing this artifact is key in capturing the natural extension of the largest avalanches and the PWL upper cutoff. Self annihilation can be delayed by carefully choosing an orthorhombic simulation box geometry. The regions of the crystals explored by an expanding loop belonging to a given slip plane are mapped using the methodology in [38]. The *extended slip plane* corresponds to the maximum extension possible for a slip system. Extended slip planes for the primary slip systems are given in the figure 10 for the box geometry optimized for i) [001], [112] and latent hardening simulations; ii) for [135] single glide conditions. The optimized geometries are a trade off between finding the largest extended plane area and the anisotropy of the geometry. We designed a larger extended slip plane for the specific [135] loading direction as dislocation mean free path is much larger in single slip condition. The paving include 1541 and 4625 polygons; the shortest radius of self-annihilation is 65 and 95 μm for geometry i) and ii), respectively.

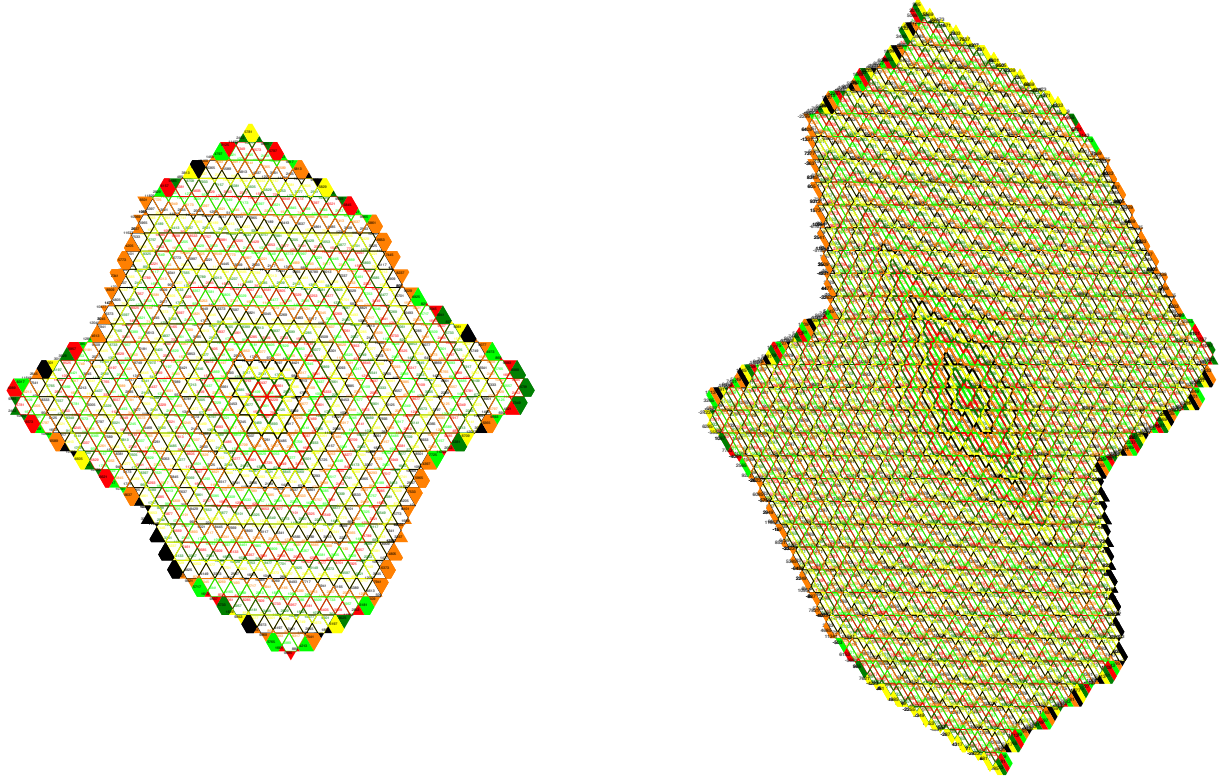


Figure 10: Mapping of the extended slip plane for the primary system used in a) multislip and latent hardening simulations conditions, b) [135] single slip conditions.

Deformation curves for various loading conditions

We considered various loading conditions to probe the anisotropy of plastic deformation, from the [135] single glide condition, [112] double slip, to [001] stable multislip condition. Latent hardening, where the forest slip system is inactive, is also considered with a forest density of 1.10^{12} m^{-2} . The initial dislocation density on active slip systems is taken as 5.10^{11} m^{-2} . The deformation curves are given in Figure 11.a). Multiplication peaks are visible for the [135] and [112] deformation curves as the initial dislocation density is not sufficient to produce the applied strain rate of 50 s^{-1} , initially. A larger peak is visible at the beginning of the latent hardening deformation but it corresponds to the stress to activate the smaller prismatic loops employed in this simulation [22]. Past these initial peaks, we recover the expected hardening rate for these loading directions. [135] deformation exhibits a hardening close to zero, in agreement with the typical value of $\mu/3000$ seen in experiments, which is too small to be seen over the range of deformation reached by DDD (A slight softening may even be possible and could be due to the microstructure development in the shape of entanglements). No hardening is expected as well for the latent hardening simulation as the forest density is fixed. Then, [112] simulation exhibit a linear hardening of the order of $\mu/300$ in agreement with macroscale experiments. Finally, [001] exhibits a linear hardening of about $\mu/150$ in agreement with initial slope seen in experimental data and the limited amount of dynamical recovery.

Figure 11.b) displays the evolution of the the total density ρ with plastic deformation using representation proposed in [11]. $\sqrt{\rho}$ scales with $\sqrt{a}\gamma/b$ when plastic deformation is balanced among active slip systems and dynamic recovery is negligible as here.

Stress resolved avalanche statistics

We also performed a stress resolved analysis of the avalanche statistics. Data are provided in Fig. 12 for [001] simulations at different initial dislocation density and Fig. 13 for various loading conditions. Avalanche

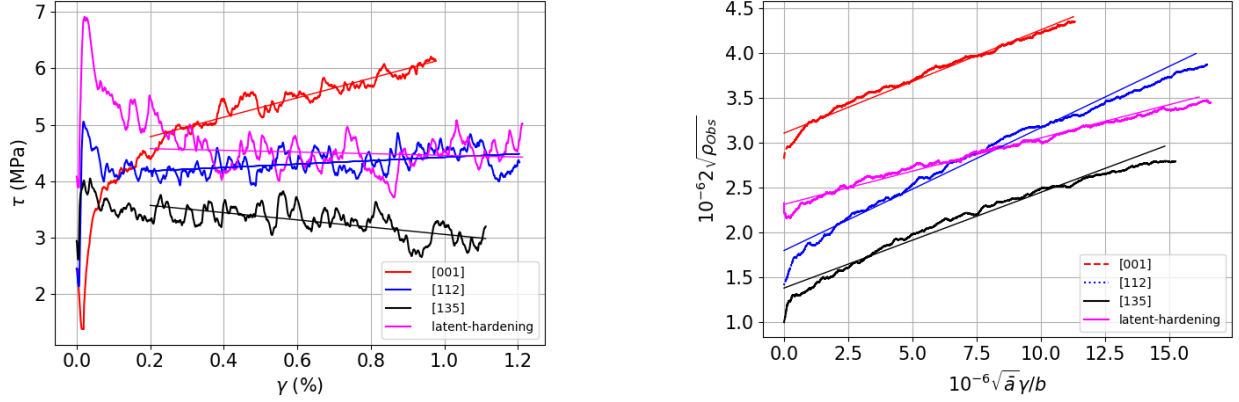


Figure 11: Plastic deformation simulated for various loading conditions. a) Deformation curves. b) Evolution of the total dislocation density as a function of plastic deformation.

statistics described by stress drops $\Delta\tau$ share many of the qualitative features of the avalanche statistics described by strain bursts $\Delta\gamma$. A well defined PWL regime can be seen over several decades of event sizes, and is delimited by cutoffs. To provide a quantitative and systematic sense of the evolution of avalanche statistics, all data were fitted using a truncated PWL equation with an exponential decay (see above). The PWL exponent is about -1.5 to -1.6 and is independent from dislocation density and loading orientation. The maximum cutoff decreases as the dislocation density increases as best seen on the CCDF curves.

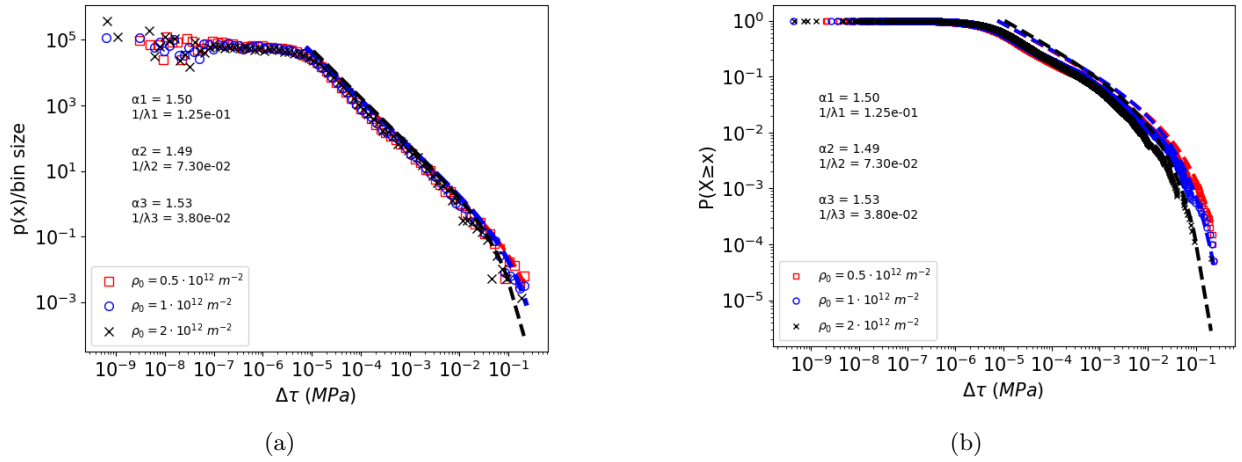


Figure 12: Impact of the initial dislocation density upon the stress resolved avalanche statistics. (a) Probability density function (PDF) of stress drops $\delta\tau$. (b) Complementary Cumulative Distribution Function (CCDF) of stress-drop $\delta\tau$

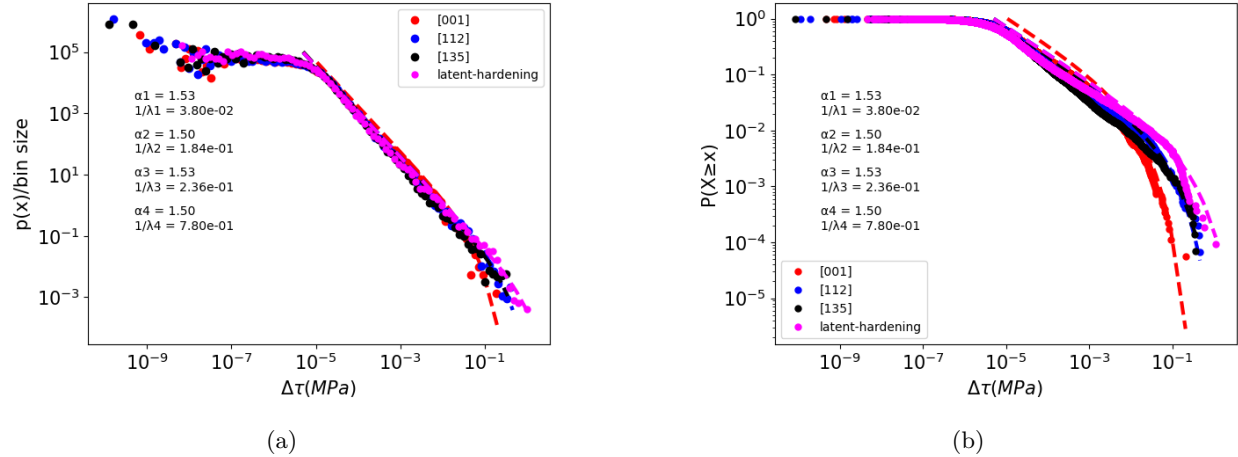


Figure 13: Impact of the loading condition upon the stress resolved avalanche statistics. (a) Probability density function (PDF) of stress-drop $\delta\tau$. (b) Complementary Cumulative Distribution Function (CCDF) of stress-drop $\delta\tau$

References

- [1] Jerome Weiss and Jean-Robert Grasso. Acoustic emission in single crystals of ice. *The Journal of Physical Chemistry B*, 101(32):6113–6117, 1997.
- [2] Thiebaud Richeton, Jérôme Weiss, and François Louchet. Breakdown of avalanche critical behaviour in polycrystalline plasticity. *Nature Materials*, 4(6):465–469, 2005.
- [3] J Weiss, W Ben Rhouma, S Deschanel, and L Truskinovsky. Plastic intermittency during cyclic loading: From dislocation patterning to microcrack initiation. *Physical Review Materials*, 3(2):023603, 2019.
- [4] Michael Zaiser. Scale invariance in plastic flow of crystalline solids. *Advances in physics*, 55(1-2):185–245, 2006.
- [5] Benoit Devincre, Thierry Hoc, and Ladislav Kubin. Dislocation mean free paths and strain hardening of crystals. *Science*, 320(5884):1745–1748, 2008.
- [6] Ferenc F Csikor, Christian Motz, Daniel Weygand, Michael Zaiser, and Stefano Zapperi. Dislocation avalanches, strain bursts, and the problem of plastic forming at the micrometer scale. *science*, 318(5848):251–254, 2007.
- [7] Dennis M. Dimiduk, Chris Woodward, Richard LeSar, and Michael D. Uchic. Scale-Free Intermittent Flow in Crystal Plasticity. *Science*, 312(5777):1188–1190, May 2006.
- [8] G Sparks and R Maaß. Nontrivial scaling exponents of dislocation avalanches in microplasticity. *Physical Review Materials*, 2(12):120601, 2018.
- [9] Jorge Alcalá, Jan Očenásek, Javier Varillas, Jaafar A. El-Awady, Jeffrey M. Wheeler, and Johann Michler. Statistics of dislocation avalanches in FCC and BCC metals: dislocation mechanisms and mean swept distances across microsample sizes and temperatures. *Scientific Reports*, 10(1):19024, 2006.
- [10] J. Weiss, W. Ben Rhouma, T. Richeton, S. Dechanel, F. Louchet, and L. Truskinovsky. From Mild to Wild Fluctuations in Crystal Plasticity. *Physical Review Letters*, 114(10):105504, March 2015.
- [11] Benoit Devincre and Ladislav Kubin. Scale transitions in crystal plasticity by dislocation dynamics simulations. *Comptes rendus. Physique*, 11(3-4):274–284, 2010.
- [12] Yinan Cui, Giacomo Po, and Nasr Ghoniem. Controlling Strain Bursts and Avalanches at the Nano- to Micrometer Scale. *Physical Review Letters*, 117(15):155502, October 2016.

- [13] G. Sparks, Y. Cui, G. Po, Q. Rizzardi, J. Marian, and R. Maaß. Avalanche statistics and the intermittent-to-smooth transition in microplasticity. *Physical Review Materials*, 3(8):080601, August 2019.
- [14] Dénes Berta, David Kurunczi-Papp, Lasse Laurson, and Péter Dusán Ispánovity. On identifying dynamic length scales in crystal plasticity. *Acta Materialia*, 283:120506, 2025.
- [15] Jaafar A. El-Awady. Unravelling the physics of size-dependent dislocation-mediated plasticity. *Nature Communications*, 6(1), May 2015.
- [16] Benoit Devincere, Ronan Madec, Ghiath Monnet, Sylvain Queyreau, Riccardo Gatti, and Ladislav Kubin. Modeling crystal plasticity with dislocation dynamics simulations: The “micromegas” code. *Mechanics of Nano-objects*, 1:81–100, 2011.
- [17] Sylvain Queyreau. Dislocation Based Mechanics: the various contributions of Dislocation Dynamics simulations. *Digital Materials: Continuum Numerical Methods at the Mesoscopic Scale*, 2024.
- [18] Wei Cai, Athanasios Arsenlis, Christopher R Weinberger, and Vasily V Bulatov. A non-singular continuum theory of dislocations. *Journal of the Mechanics and Physics of Solids*, 54(3):561–587, 2006.
- [19] Athanasios Arsenlis, Wei Cai, Meijie Tang, Moono Rhee, Tomas Opperstrup, Gregg Hommes, Tom G Pierce, and Vasily V Bulatov. Enabling strain hardening simulations with dislocation dynamics. *Modelling and Simulation in Materials Science and Engineering*, 15(6):553, 2007.
- [20] S Queyreau, J Marian, BD Wirth, and A Arsenlis. Analytical integration of the forces induced by dislocations on a surface element. *Modelling and Simulation in Materials Science and Engineering*, 22(3):035004, 2014.
- [21] Benoit Devincere, Ladislav Kubin, and Thierry Hoc. Physical analyses of crystal plasticity by dd simulations. *Scripta materialia*, 54(5):741–746, 2006.
- [22] Sylvain Queyreau, Ghiath Monnet, and Benoît Devincere. Slip systems interactions in α -iron determined by dislocation dynamics simulations. *International Journal of Plasticity*, 25(2):361–377, 2009.
- [23] Ladislav Kubin. *Dislocations, mesoscale simulations and plastic flow*, volume 5. Oxford University Press, USA, 2013.
- [24] L Kubin, T Hoc, and B Devincere. Dynamic recovery and its orientation dependence in face-centered cubic crystals. *Acta Materialia*, 57(8):2567–2575, 2009.
- [25] Sylvain Queyreau and Benoit Devincere. A multiscale investigation of the physical origins of tension–compression asymmetry in crystals and their implications for cyclic behavior. *arXiv preprint arXiv:2112.15481*, 2021.
- [26] Haidong Fan, Qingyuan Wang, Jaafar A El-Awady, Dierk Raabe, and Michael Zaiser. Strain rate dependency of dislocation plasticity. *Nature communications*, 12(1):1845, 2021.
- [27] Aaron Clauset, Cosma Rohilla Shalizi, and Mark EJ Newman. Power-law distributions in empirical data. *SIAM review*, 51(4):661–703, 2009.
- [28] Sv Takeuchi and E Kuramoto. Temperature and orientation dependence of the yield stress in ni {in3} ga single crystals. *Acta metallurgica*, 21(4):415–425, 1973.
- [29] Sh Akhondzadeh, Nicolas Bertin, Ryan B Sills, and Wei Cai. Slip-free multiplication and complexity of dislocation networks in fcc metals. *Materials Theory*, 5:1–24, 2021.
- [30] Benoît Devincere, L Kubin, and Thierry Hoc. Collinear superjogs and the low-stress response of fcc crystals. *Scripta Materialia*, 57(10):905–908, 2007.
- [31] Ryan B Sills, Nicolas Bertin, Amin Aghaei, and Wei Cai. Dislocation networks and the microstructural origin of strain hardening. *Physical review letters*, 121(8):085501, 2018.

- [32] G Saada. Interaction de dislocations érouissage et production de défauts ponctuels dans les métaux cfc. *Acta Metallurgica*, 9(2):166–168, 1961.
- [33] R Madec, Benoit Devincre, and Ladislav P Kubin. From dislocation junctions to forest hardening. *Physical review letters*, 89(25):255508, 2002.
- [34] UF Kocks and H Mecking. Physics and phenomenology of strain hardening: the fcc case. *Progress in materials science*, 48(3):171–273, 2003.
- [35] L Kubin, B Devincre, and T Hoc. Modeling dislocation storage rates and mean free paths in face-centered cubic crystals. *Acta materialia*, 56(20):6040–6049, 2008.
- [36] David Kurunczi-Papp and Lasse Laurson. Avalanches and rate effects in strain-controlled discrete dislocation plasticity of al single crystals. *Physical Review Materials*, 7(1):013605, 2023.
- [37] M-Carmen Miguel, Alessandro Vespignani, Stefano Zapperi, Jérôme Weiss, and Jean-Robert Grasso. Intermittent dislocation flow in viscoplastic deformation. *Nature*, 410(6829):667–671, 2001.
- [38] Ronan Madec, Benoit Devincre, and Ladislav Kubin. On the Use of Periodic Boundary Conditions in Dislocation Dynamics Simulations. In G. M. L. Gladwell, H. Kitagawa, and Y. Shibutani, editors, *IUTAM Symposium on Mesoscopic Dynamics of Fracture Process and Materials Strength*, volume 115, pages 35–44. Springer Netherlands, Dordrecht, 2004.